Structure of the Los Angeles Basin From Multimode Surface Waves and H/V Spectral Ratio

Gregory C. Beroza[1], Mathieu Perton[2] and Zack J. Spica[1]

[1]CONACYT, Instituto de Geofísica UNAM, Unidad Michoacán, Antigua Carretera a Pátzcuaro 8701, 58190, Morelia, Michoacán, Mexico.

[2]Department of Geophysics, 397 Panama Mall, Stanford University, Stanford, California 94305-2215, USA.

Corresponding author: Zack Spica, `zackspica@gmail.com`

Abstract

We use broadband stations of the 'Los Angeles Syncline Seismic Interferometry Experiment' (LASSIE) to perform a joint inversion of the Horizontal to Vertical spectral ratios (H/V) along with multimode dispersion curves (phase and group) for both Rayleigh and Love waves at each station of the dense line of sensors. The H/V of the auto-correlated signal at a seismic station is proportional to the ratio of the imaginary parts of the Green's function. The presence of low frequency peaks (~0.2 Hz) in the H/V allows us to constrain the structure of the basin with high confidence to a depth of 6 km. The velocity models we obtain are broadly consistent with the SCEC CVM-H community model. Because our approach differs substantially from previous modeling of crustal velocities in southern California, this research validates both the utility of the diffuse field H/V measurements for deep structural characterization and the predictive value of the CVM-H community velocity model in the Los Angeles region. A lower frequency peak (~ 0.03 Hz) in H/V allows also retrieving the Moho depth. Finally, we show that the independent comparison of the H and V components with their corresponding theoretical counterparts give information about the degree of diffusivity of the ambient seismic field.

1 Introduction

Much of metropolitan Los Angeles (Fig 1) is situated atop sedimentary basins. The Los Angeles Basin (LAB) is the largest of these and understanding its seismic response is of fundamental importance for mitigating the risk caused to one of the most densely populated region in the US. Sedimentary basins are known to influence dramatically damage from earthquake shaking by increasing the amplitude and duration of ground motion, and

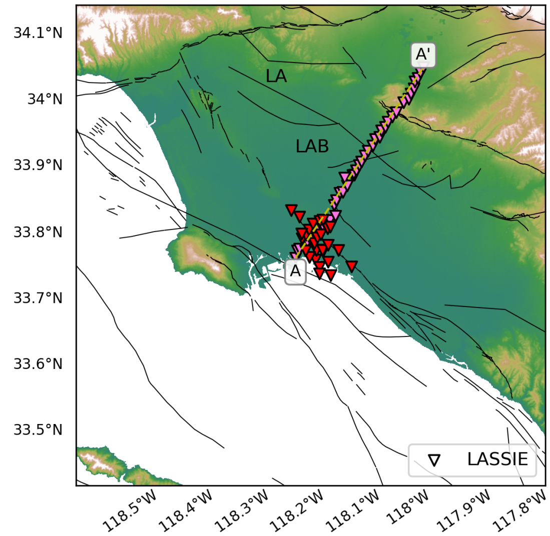

Figure 1. The LASSIE array and the Los Angeles basin area. The red and pink triangles are the broad-band stations of the LASSIE 1 and LASSIE 2 arrays, respectively. Only the structures below the 43 stations of the linear array are assessed. The yellow dashed line denotes the location of the profile A–A'. The faults are shown in black lines [from *Jennings and Bryant*, 2010]. LA: Los Angeles; LAB: Los Angeles Basin.

by responding nonlinearly to incident seismic waves [e.g. *Cruz-Atienza et al.*, 2016]. Multiple ground motion simulation efforts [*Olsen*, 2000; *Olsen et al.*, 2006, 2009; *Komatitsch et al.*, 2004; *Graves et al.*, 2011], along with independant ambient-field measurements [*Denolle et al.*, 2014] have confirmed such behavior for the Los Angeles Basin, especially in the 2-5 s period range, which poses a substantial risk to tall buildings and other long-period structures. The predictive value of simulations depends critically on the accuracy of structural representations of these basins [e.g. *Wald and Graves*, 1998], which motivates continuing effort to constrain their structure.

Significant progress has been made toward the goal of developing a unified velocity structure for Southern California. Special emphasis on the Los Angeles region started initially with data from the energy industry [e.g. *Wright*, 1991], which continues to provide data [e.g. *Nakata et al.*, 2015]. *Magistrale et al.* [2000] used a combination of receiver functions [*Zhu and Kanamori*, 2000], geotechnical data [*Magistrale et al.*, 1996] and tomography [*Hauksson*, 2000] to produce first such unified model, known as CVM-S. To determine the shape of the sedimentary section of the LAB, *Süss and Shaw* [2003] used *P*-wave velocity measurements derived from stacking velocities obtained from reflection surveys and calibrated them with numerous sonic logs from boreholes. These models were spliced together and further refined through full-waveform inversion [*Tape et al.*, 2009; *Lee et al.*, 2014], leading to a unified model [*Shaw et al.*, 2015] : the SCEC Community Velocity Model - Harvard (CVM-H, latest version 15.1.0).

Because the ambient seismic field (ASF) can be measured wherever seismic stations are located, and at whatever density they are deployed, it is playing an increasingly important role in constraining the crustal structure [*Shapiro et al.*, 2005; *Lin et al.*, 2013; *Bowden et al.*, 2015; *Nakata et al.*, 2015; *Ma and Clayton*, 2016]. With dense arrays, both high-frequency surface waves [e.g. *Lin et al.*, 2013; *Spica et al.*, 2018b] and body waves [*Nakata et al.*, 2015; *Spica et al.*, 2018b] can be extracted, and used to determine the velocities in shallow crust. The high-frequency surface waves extracted from ASF are often composed of both fundamental and higher modes [e.g. *Spica et al.*, 2018b,a; *Savage et al.*, 2013; *Tomar et al.*, 2018; *Rivet et al.*, 2015; *Ma et al.*, 2016], which means they are rich in information, but that potential points of osculation (touching) in the dispersion curves (DC) can compromise their correct identification [*Spica et al.*, 2018a]. *Ma et al.* [2016] used the 'Los Angeles Syncline Seismic Interferometry Experiment' array (LASSIE; Fig.

1; *LASSIE* [2014]) to show that higher modes are a strong component of high-frequency Rayleigh waves. They proposed that their separation can be performed through a particle motion filter. In a companion paper *Ma and Clayton* [2016] used the fundamental mode of both Love and Rayleigh wave along with receiver-function analysis to provide new constraints on the 2-D V_S structure of the LAB. They highlighted that the shallow structure (less than 10 km depth) present strong lateral variations near fault lines, which might have significant impact on seismic wavefield.

In addition to the use of long-range correlation between pairs of stations, *Sánchez-Sesma et al.* [2011] showed that a single three-component short-time measurements of ASF can be used to directly assess the geological structure through the Horizontal-to-Vertical spectral ratio (HVSR or H/V) [e.g. *Spica et al.*, 2015; *García-Jerez et al.*, 2016; *Piña-Flores et al.*, 2016; *Perton et al.*, 2017]. While H/V is traditionally considered to be only sensitive to the shallow-surface (i.e. the first 200m) [*Nakamura*, 1989], recent studies demonstrated the feasibility of using it to image deep interfaces down to several kilometers [*Spica et al.*, 2015, 2018a]. One well-known problem is that H/V measurement at the surface is generally insufficient to characterize soil properties because a proportional change in layer velocities and thicknesses leads to similar H/V [e.g. *Piña-Flores et al.*, 2016]. Independent information, such as surface wave dispersion [*Scherbaum et al.*, 2003; *Piña-Flores et al.*, 2016; *Lontsi et al.*, 2016] or H/V measurements recorded at different depths [*Lontsi et al.*, 2015; *Spica et al.*, 2017b] or locations [*Perton et al.*, 2017] all provide opportunities to reduce this non-uniqueness. Additionally, *Perton et al.* [2017] also suggested that the *H* and *V* components could be considered independently to better assess the H/V and to characterize some properties of the noise field illumination.

Surface DC extracted from the ASF are sensitive to the absolute velocity and using several modes provide different depth sensitivity giving further constraints on the velocity model [*Tomar et al.*, 2018; *Spica et al.*, 2018a]; however, dispersion analysis may also suffer from their own non-uniqueness due to mode miss-identification and its trend to smooth the model properties along depth. H/V is primarily sensitive to sharp shear wave velocity contrasts and vertical travel-times, which offers a complimentary sensitivity that helps to map sharp interfaces.

We use data from the LASSIE array, which is a relatively dense array of 71 broadband sensors that traversed the Los Angeles Basin [*LASSIE*, 2014]. Fig. 1 shows the location of the temporal experiments in which 43 stations were deployed in a line with ~1 km inter-station distance (i.e., LASSIE 2). Stations recorded continuous seismic wavefields for about 40 days starting in September 2014. We provide a 2-D V_S profile of the Los Angeles Basin down to 6 km depth by means of a novel joint inversion procedure that involves H/V, multi-mode Love- and Rayleigh-wave dispersion at each station of the linear array and therefore provides some additional constraints on the shear wave velocity structure of the basin. Finally, we demonstrate that deep lithospheric characterization using H/V by showing that H/V frequency peaks under 0.1 Hz are sensitive to the Moho discontinuity.

2 Data processing

A traditional approach to infer the V_S structure under a station of a linear array using ASF would be to pursue surface wave tomography at different periods and then invert a localized 1-D DC obtained at the closest grid point from the station [e.g. *Ma and Clayton*, 2016]. This approach can be applied for both Rayleigh and Love waves. As discussed in *Ma and Clayton* [2016], the energy on the Rayleigh waves in the Los Angeles Basin may spread over several overtones while the modal content of the Loves waves is simpler. The application of the Rayleigh wave tomography requires a careful mode identification in the frequency-time diagrams. *Ma and Clayton* [2016] proposed to use the retrograde ellipticity of the Rayleigh wave as a time-domain filter to isolate the fundamental modes of the GF and use them for tomography; however, when the velocity structure has a strong velocity-density gradient, the Rayleigh fundamental mode can switch to prograde ellipticity [*Tanimoto and Rivera*, 2005; *Denolle et al.*, 2012], making the time-domain filter approach ambiguous. More complications appear at osculation points where energy leaks between modes and where the time-domain filter becomes inefficient.

We propose an alternative blind multi-mode identification in the frequency-velocity diagrams computed from local correlation functions computed by [*Ma and Clayton*, 2016]. As described in *Spica et al.* [2018a], this approach avoids mode selection and better samples local heterogeneities than regionalized 1-D DC from tomographic inversion, which tends to smooth heterogeneities.

At a given station S, we select all the correlation functions from station-pairs located inside an area of 15 km radius centered on S. We use all the stations from the LASSIE 1 and 2 experiments in Fig. 1. For each station pair of inter-station length L, the center of the segment L must be distant from S by at most $D < L/6$ (except at both ends of the linear array where the selection criterion is lowered at $L/2$) to ensure that S is close to the center of the segment and then to be only sensitive to local heterogeneities. We apply a frequency-time analysis (FTAN) to all the selected correlation functions and to avoid averaging the media properties over several wavelengths we consider only data satisfying $L/2 < \lambda = \frac{c}{f} < 1.25L$. Only the most energetic contributions for each frequency are selected to avoid spurious arrivals. The prominent arrivals are plotted together on a frequency versus velocity diagram. This tends to select the fundamental mode of the Rayleigh wave for the shortest inter-station distance and higher-modes for larger inter-station distances. For the Love waves, the fundamental mode is generally the strongest [*Ma and Clayton*, 2016] and only a few points are associated with higher modes or artifacts caused by, for example, reflections from lateral heterogeneity. Our approach is to consider all possible modes in the inversion process to fit as many data as possible and to improve the constraints on the depth-dependence of the velocity model.

An example of the blind selection is shown in Fig.2 for station XI-N117. Clear curves emerge from the scatter above 0.2 Hz, with a large dispersion of the measurements observed below this frequency. These points might be caused by the presence of several modes, by horizontal anisotropy or by local lateral heterogeneity. In order to avoid converging to isolated points, we further filter these data by averaging them in frequency and in velocity, and by selecting at each frequency only the three clouds of points with highest density. The result of the average is shown as empty circles in Figs.2 B and D.

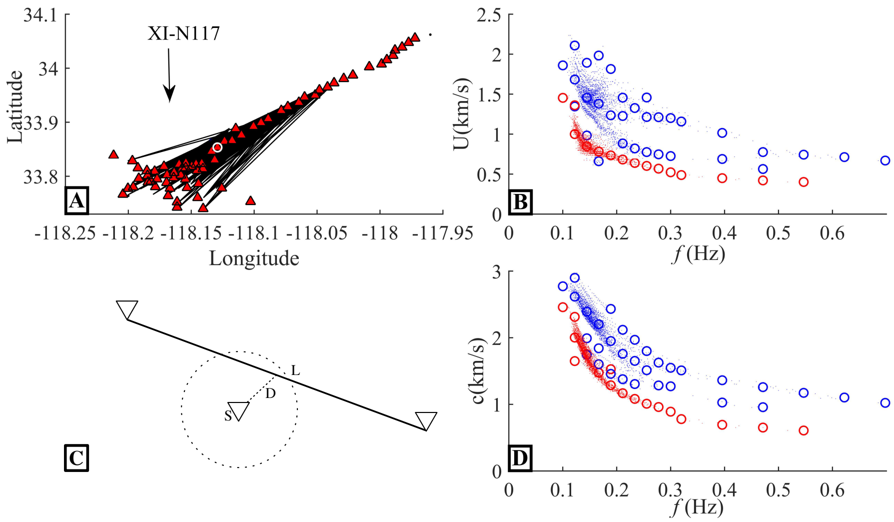

Figure 2. **A)** All the LASSIE stations (red triangles) and selected station pairs (black rays) around station XI-N117 (white circle) for the DC selection. Group (**B**) and phase (**D**) frequency-velocity diagrams. The original measured velocity from FTAN are depicted as small blue and red points for Rayleigh and Love waves, respectively. The frequency-velocity average of these scattered point-clouds are depicted as empty circles of the same colors.

2.1 H/V analysis

Following *Sánchez-Sesma et al.* [2011], we interpret the H/V spectral ratio in terms of the imaginary part of the GF:

$$\frac{H}{V}(\mathbf{x},\omega) = \sqrt{\frac{\langle |v_1(\mathbf{x},\omega)|^2\rangle + \langle |v_2(\mathbf{x},\omega)|^2\rangle}{\langle |v_3(\mathbf{x},\omega)|^2\rangle}} = \sqrt{\frac{\mathrm{Im}(\mathcal{G}_{11}(\mathbf{x},\omega) + \mathcal{G}_{22}(\mathbf{x},\omega))}{\mathrm{Im}(\mathcal{G}_{33}(\mathbf{x},\omega))}}. \tag{1}$$

Where $v_i(\mathbf{x},\omega)$ is the particular velocity spectrum component in the direction i when source and receiver are superimposed at x and for frequency $f = \omega/2\pi$. Components 1 and 2 are in the horizontal plane while component 3 is in the vertical. The symbol $\langle\rangle$ denotes the average over multiple time windows. The expression $|v_i(\mathbf{x},\omega)|^2$ is proportional to the directional energy densities ($E_i = \rho\langle |v_i(\mathbf{x},\omega)|^2\rangle$) [*Perton et al.*, 2009] in direction i and corresponds to the average autocorrelations of the ASF, which under a diffuse field assumption are proportional to the imaginary part of the GF components ($\mathrm{Im}(\mathcal{G}_{ii})$). They are therefore treated as classical ASF cross-correlations, but for the special case when the source and receiver are superimposed. $\mathcal{G}_{ii}(\mathbf{x}, \omega)$ is the displacement GF in the direction i at a point $\mathbf{x}$ due to the application of a unit point force in the direction i at the point $\mathbf{x}$.

Because we are interested in the deep velocity structure of the basin and its geometry, we seek to retrieve low-frequency peaks in H/V. Under the equipartition theorem, the low frequencies are theoretically retrieved more rapidly than the high frequencies [*Perton and Sánchez-Sesma*, 2016]. Indeed, a diffuse field can be seen as a superposition of plane waves with propagation directions that cover all available space directions. At low frequency, the wavelengths are larger than at high frequency and fewer waves are required to span all the directions effectively. In practice, however, these frequencies may not always be well retrieved since the ASF may be non-diffuse [e.g., *Liu and Ben-Zion*, 2017]; noise sources or secondary sources such as scatterers are not isotropically distributed. Appropriate signal processing, which includes larger time windows and long-time averaging must be applied to obtain stable and reliable low-frequency peaks in H/V.

For each ASF record, we select time windows of 500 s. Each window is tapered by a 5% cosine function to suppress strong frequency leakage, de-meaned, de-trended, bandpass filtered from 0.05 to 2 Hz, and overlapped by 90%. We apply spectral whitening to each window to enhance equipartitioning of the wavefield [e.g *Bensen et al.*, 2007]. Because different sources will act in different frequency bands, the whitening consists of normalizing the signals by the source energies computed from the three components in each time window (i.e. source deconvolution) across different frequency bands [*Perton et al.*, 2017] as:

$$\tilde{v}_i(\mathbf{x}, \omega) = v_i(\mathbf{x}, \omega) / \sqrt{\sum_{i=1}^{3} |v_i(\mathbf{x}, \Delta\omega)|^2}. \quad (2)$$

$\Delta\omega$ is the frequency band centered on ω considered to calculate the energy. It is taken frequency dependent as $\Delta\omega = \omega/2$ because the frequency band is relatively large in this study (i.e., 0.01 to 2 Hz) and because the peaks in the H/V spectra have almost the same width when plotted on a logarithmic frequency axis [*Piña-Flores et al.*, 2016]. This bandwidth is taken larger than the width of the peaks of the directional energies and narrow enough to remove the spectral envelope due to the seismic sources (see Fig. 3).

We compute the autocorrelation of each time window as the square of the absolute value in frequency and average over several days. Tests revealed that 5 days of data gives essentially the same results than using 40 days. The directional energies for station XI-N101 are presented in the figure 3. The two horizontal directional energies are similar above 0.1 Hz but differ below that frequency. Although this could be explained by the presence of heterogeneities or topography that reflects the energy, the main effect is certainly the non-isotropic ASF illumination. The shear velocities of the CVM-H model are higher than 1 km/s for depths sampled by frequencies below 0.1 Hz such that the corresponding wavelengths are at least 10 km. At such scale, the coast can be considered as a straight line and the ASF generated from the interaction between the ocean and the coast should be highly unidirectional (see Fig. 1), [e.g., *Roux and Ben-Zion*, 2017]. In fact, the largest difference between the two horizontal energy densities is obtained by rotating them by an angle of 5 degrees clockwise, i.e. the South-North components show

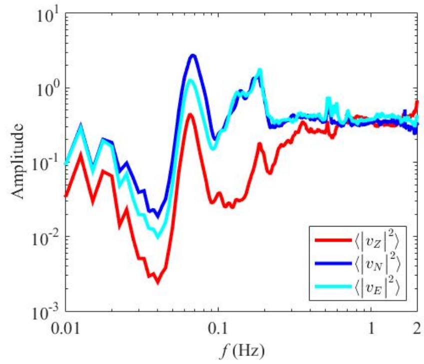

Figure 3. Directional energies at station XI-N101.

higher amplitude, which is consistent with the fact that close to Long Beach (point A), the shore is nearly East-West. The ratios between the horizontal components at low frequency (<0.1Hz) vary for all the stations of LASSIE 1 (red triangles in Fig.1) and reach up to a factor of 4 for some locations and some frequencies; however, for inland stations, the two horizontal components show similar amplitude, suggesting a more homogeneous ASF source illumination [e.g., *Liu and Ben-Zion*, 2017].

Additionally, as discussed in *Perton et al.* [2017], the directional energies are equals to the imaginary part of the GF times a factor of frequency raised to a power of D, which depends on the ASF illumination: $E_i \propto -f^D \mathrm{Im}(\mathcal{G}_{ii})$ with $D = 1$ when the field is diffuse in three dimensions (3D) and $D = 2$ in two dimensions (2D). The comparison of the individual components

$$\begin{cases} H = \sqrt{E_1 + E_2} \\ V = \sqrt{E_3} \end{cases} \quad \text{with} \quad \begin{cases} \sqrt{-f^D \mathrm{Im}(\mathcal{G}_{11} + \mathcal{G}_{22})} \\ \sqrt{-f^D \mathrm{Im}(\mathcal{G}_{33})} \end{cases} \tag{3}$$

can be used to identify the factor D in different frequency band as discussed in section 5.

Finally, the H/V measurements are obtained by applying eq. 1. Three H/Vs are shown in Fig. 4A, as well as their upper and lower bounds calculated from the maximum and minimum values at each frequency of the auto-correlations computed with half of the total number of windows.

The narrow confidence intervals for frequencies above 0.1 Hz (see Fig. 4A) demonstrate the good convergence of the H/V after stacking [e.g. *Spica et al.*, 2017b]. The quality of H/V retrieval in this frequency band is further verified by the spatial continuity of the spectral H/V amplitude along the line A–A' (Fig. 4C) and where we observe that the H/V shapes change smoothly from station to station. We only observed a discontinuous variation (anomalous high amplitude above 0.1Hz and low amplitude below 0.1 Hz) near Whittier. As discussed, in section 4, this feature might result from topographic effects generating interference between incident surface-waves and their reflections. Because we assume a local 1D structure during the inversion, topographic effects on H/V [e. g., *Molina-Villegas et al.*, 2018; *Maufroy et al.*, 2018] are beyond the scope of this paper.

The observed confidence intervals are large below 0.1 Hz in (Fig. 4A), even with 40 days of record. The lack of convergence is unrelated to the number of windows used, not is this due to the difference between the two horizontal energy densities. Instead, we explain this by the presence of an anomalous feature between 0.04 and 0.06 Hz, either positive either negative in Fig. 4A. We also highlighted this discontinuity in amplitude in Fig. 4C by a red dashed rectangle. This feature comes from very strong oscillations in the energy densities (Fig. 3), highlighting the power of the H/V technique to suppress the effect of ASF anomalies in the energy densities. We will return to this point in section

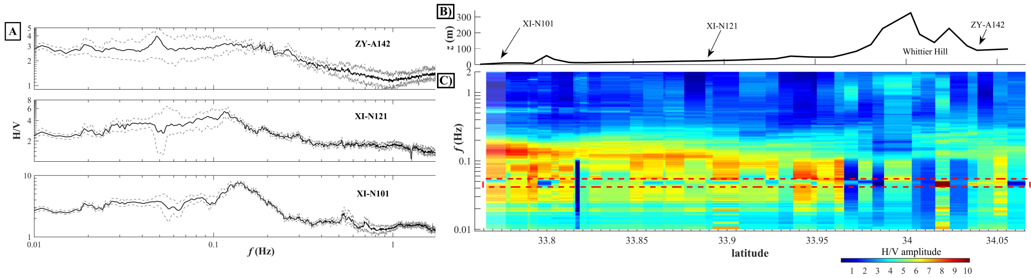

Figure 4. A: Three examples of H/V calculated at stations XI-N101, XI-N121 and ZY-A142 with their respective upper and lower bounds. B: Elevation at seismic stations along the same line. C: Amplitude representation of all the H/V along the line A–A' presented in Fig. 1 and in function of frequency. The red dashed rectangle highlights an anomalous amplitude .

5. We suppose the origin of the oscillations might be related to strong non-diffuse nature of the wavefield observed below 0.1 Hz [*Liu and Ben-Zion*, 2017]. For these reasons, we decided to carry out the H/V inversion for a bandwidth between 0.1 and 2 Hz.

3 1-D joint inversion

Individually, the inversion of H/V or of the DC lead to non-unique solutions [e.g. *Piña-Flores et al.*, 2016], but this non-uniqueness can be reduced significantly by inverting these measurements jointly, due to their complementary sensitivity [e.g. *Arai and Tokimatsu*, 2004; *Parolai et al.*, 2005; *Zor et al.*, 2010; *Dal Moro*, 2011; *Piña-Flores et al.*, 2016; *Lontsi et al.*, 2016; *Spica et al.*, 2018a].

H/V is weakly sensitive to the absolute velocity but carries information on relative velocity levels, and is particularly sensitive to V_S contrasts. It is also a local measurement sampling the structure along an essentially vertical path under the station. On the other hand, the DC are sensitive to the absolute velocity variation with depth, but are only sensitive to velocities averaged in their sensitivity kernels. The joint inversion of several modes of group (U) and phase (c) velocities should increase depth resolution [e.g., *Dziewonski and Anderson*, 1981]. Even if group (U) and phase (c) velocities are theoretically related, their joint inversion for shear wave structure gives notably better results than either one individually [e.g., *Shapiro and Ritzwoller*, 2002; *Spica et al.*, 2017a]. Because the velocities U and c are computed separately, they allow a consistency check and are therefore used as independent data with different sensitivity. The DC are the expression of a lateral averaging of the structure below the small sub-arrays used for their computation, and this effect can be managed through the DC selection process. In contrast to the waves probed with the H/V technique, the surface wave propagation expressed in the DC by separated seismic stations have an essentially horizontal wave vector.

In summary, the DC and H/V provide complementary measurements to reduce the non-uniqueness of the velocity variation with depth and are sensitive to distinct aspects of the structure.

3.1 Forward calculation

The $\mathrm{Im}(\mathcal{G}_{ii})$ components on the right hand side of eq. 1 are associated with an assumed locally horizontal layered structure that varies only with depth. We use the discrete wave number (DWN) method [*Bouchon*, 2003] for the theoretical calculation of the H/V [e.g. *Sánchez-Sesma et al.*, 2011; *Spica et al.*, 2017b; *Perton et al.*, 2017] and the scheme presented by *Perton and Sánchez-Sesma* [2016] for the DC computation.

As in [*Spica et al.*, 2018a], the bandwidth of the H/V considered in this study spans almost two orders of magnitude with H/V peaks at both low and high frequencies (Fig 4). Proper fitting of the entire spectrum would require a large number of layers to represent the entire velocity profile. The resulting large number of degrees of freedom introduces numerical instabilities in the GF calculation [*Perton and Sánchez-Sesma*, 2016], and considerably slows the inversion. To address these issues we simplify the representation of the velocity structure at each frequency considered during inversion according to the body and surface wave wavelengths and reduce it at the depth for which there is little sensitivity (typically five times the surface wave wavelength) [*Perton et al.*, 2017; *Spica et al.*, 2018a]. For this reason, at high frequency, only the shallow part of the structure is considered and at low frequency the smaller, shallow layers are merged while conserving wave propagation times.

3.2 Objective function

Joint inversion of the measurements presents several challenges because we must capture the available information in both the DC and H/V through appropriate weighting [e.g. *Spica et al.*, 2018a]. Furthermore, DC and H/V have different units, sampling rate, and scaling. Furthermore, because the Rayleigh and Love modes are of variable quality, the number of modes extracted varies from one site to another. Definition of an appropriate objective function is therefore an important step in converging to stable results. Adding constraints, particularly accurate prior information (if available), can help regularize the problem.

At each station, the misfit function includes the group (U) and phase (c) velocity DC for the fundamental (index 0) and higher-modes (index $n > 0$) Rayleigh wave and only the fundamental Love wave, as well as $^{H}/_{V}$ measurements to estimate the shear velocities and layer thicknesses. We seek to minimize the objective function ε, given by:

$$\varepsilon = \sqrt{\frac{C^{HV}}{N^{HV}} \sum_{f_{min}^{HV}}^{f_{max}^{HV}} \left(\frac{{}^{H}\!/\!{}_{V}^{obs}(f) - {}^{H}\!/\!{}_{V}^{th}(f)}{{}^{H}\!/\!{}_{V}^{obs}(f)} \right)^2 + \frac{C^{DC}}{N^{DC}} \sum_{f_{min}^{DC}}^{f_{max}^{DC}} \left(\begin{array}{l} \sum_{n_{Ray}=0}^{2} F^2 \left(U_{Ray}^{obs}(f) - U_{n_{Ray}}^{th}(f) \right) + \\ \sum_{n_{Ray}=0}^{2} F^2 \left(c_{Ray}^{obs}(f) - c_{n_{Ray}}^{th}(f) \right) + \\ F^2 \left(U_{Love}^{obs}(f) - U_{n_{Love}=0}^{th}(f) \right) + \\ F^2 \left(c_{Love}^{obs}(f) - c_{n_{Love}=0}^{th}(f) \right) \end{array} \right)} \tag{4}$$

with

$$F(x) = \begin{cases} x, & \text{if } x < \text{threshold} \\ \text{threshold} - x, & \text{if threshold} < x < 2\text{threshold} \\ 0, & \text{otherwise} \end{cases}$$

Observed versus theoretical quantities are denoted by the superscripts ^{obs} and th, respectively. The normalization factors C_{HV} and C_{DC} were adjusted to control the relative influence of H/V versus DC in the analysis. Here a higher weight is given to H/V to emphasize vertical layering and the dispersion curves as a sort of regularization to reduce non-uniqueness. N^{HV} and N^{DC} are the number of frequencies, which are sampled logarithmically and linearly respectively between the frequency bounds f_{min} and f_{max}. Because we carry out no explicit mode identification, the input data for dispersion curve are not interpolated and only data points close to the frequency sampled by the theoretical curves are considered [*Spica et al.*, 2018a].

3.3 Parameterization

The only free parameter considered is the shear wave velocity V_S. We focus on estimating only this parameter for several reasons. Both Love and Rayleigh wave DC are more sensitive to V_S than to other parameters. This is true for H/V as well [*Spica et al.*, 2015]. Moreover, strong ground motion prediction is most strongly dependent on the shear-wave velocity structure. The density and the compressional wave velocity are assessed to be related to V_S through empirical relationships of polynomial form [*Berteussen*, 1977; *Brocher*, 2005].

Because the V_S model from CVM-H being smoothed and proposed with more than hundred of layers we harmonically averaged the model to reduce the unknown and use it as a starting velocity model for the first inversion. We then switch to the closest profile resulting from our inversion for the other locations. We use a constrained nonlinear optimization procedure [gradient method; *Byrd et al.*, 1999]) to minimize the misfit (ε); however, when considering a large number of layers, the sensitivity to the parameters decreases. To reduce this effect, the inversion is performed iteratively following the approach described in *Spica et al.* [2016] – i.e., a layer is inserted between the two layers showing the highest sensitivity (misfit variation for a given velocity variation) – and we estimate only the parameters of the five surrounding layers (two on each side of the inserted layer). This process is repeated iteratively until an acceptable misfit ($\leq$5), or a maximum number of iterations (10) is reached. Finally, we limit the velocity difference to 25% between adjacent layers.

4 Results and discussion

4.1 Testing the inversion at station XI-N117

Although the joint inversion increases the number of constraints the identification of a satisfying model that fits all the measurements is not guaranteed. As an example, we show in figure 5 the associated DC and H/V for station XI-N117 calculated from the CVM-H model at the same position. The three first Rayleigh's modes fit some of the targets in the frequency band 0.1–1 Hz and the H/V also matches for the whole spectrum (0.02–2 Hz). However there are three issues regarding the DC. First, the theoretical Love DCs (brown lines) are all far from the measurements (red points). Second, the third Rayleigh's mode does not fit the measurements below 0.5 Hz for phase velocity and below 0.2 Hz for group velocity. Third, according to the theoretical phase velocity frequency diagram for this velocity structure, the first phase Rayleigh mode should be strong across the whole frequency band (see Fig. 6); however we do not retrieve measurements for this mode above 0.2 Hz in the FTAN.

To address these issues, we first conducted an isotropic inversion, following the modes identified in figure 2, but we were unable to reduce the misfit. In a second attempt, we introduced anisotropy and conducted an inversion of the Love DC independently from the Rayleigh's DC as in *Ma and Clayton* [2016] and *Spica et al.* [2017a] without considering the H/V; however, this led to unreliable results with unreasonably strong high anisotropy (note that such approaches are only valid for weak anisotropy [*Xie et al.*, 2013]).

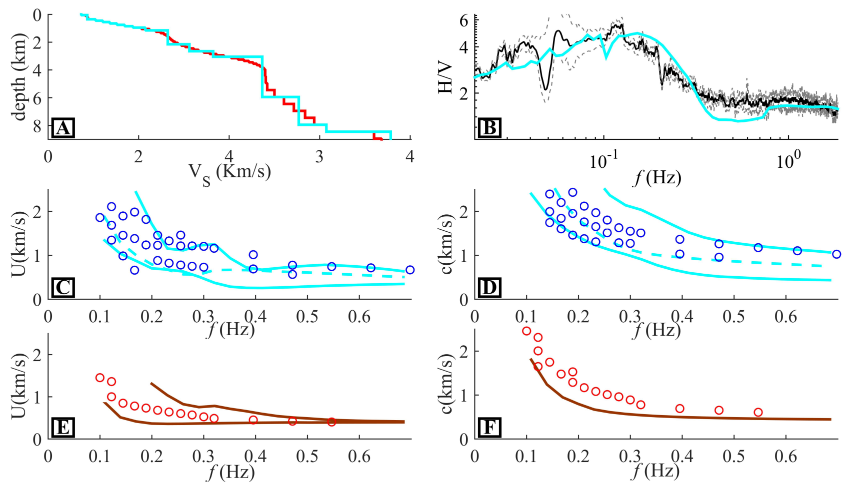

Figure 5. Observed DC and H/V and their theoretical counterpart computed from the CVM-H model at station XI-N117. **A)** CVM-H V_S model (red) under station XI-N117 and harmonically averaged CVM-H V_S model (cyan) used to compute the theoretical H/V and DCs. **B)** Experimental H/V (black line) with its lower and upper bounds (gray lines) and theoretical H/V (cyan). Group (**C**) and phase (**D**) frequency-velocity diagrams for RayleighâĂŹs waves (blue circles) and group (**E**) and phase (**F**) frequency-velocity diagrams for LoveâĂŹs waves (red circles). Theoretical DCâĂŹs are also shown in cyan lines for Rayleigh waves (the second mode is shown as a dashed line to help its identification) and in brown lines for Love's modes.

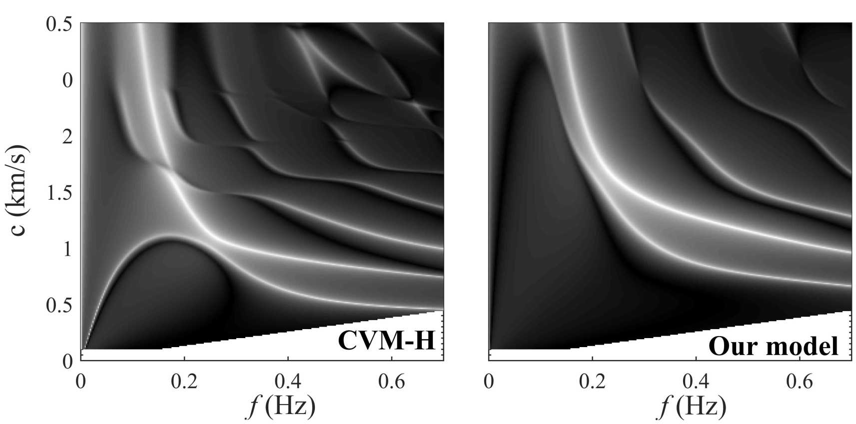

Figure 6. Phase velocity diagrams (c, f) computed from the CVM-H model (left) and our best optimized model (right). The two panels were obtained by simulating the wave propagation with the DWN method. Since, the light shades are associated with higher energy comparing to dark shades, the lines correspond to the dispersion curves.

Despite the good fits observed on the DC and H/V when using the CVM-H model, we conducted an inversion without prior mode identification. We obtained the agreement to the data shown in Fig. 7. The H/V agreement is excellent, particularly for frequencies above 0.3 Hz. Rayleigh and Love mode phase velocities fit better with the targeted points, and the improvement is apparent at low frequencies compared to the DC associated to CVM-H model. We observe that the velocity gradient of our model is similar to the CVM-H reference model; however, the Rayleigh wave modes are switched: the fundamental (f_0) and first higher modes (f_1) are rarely superimposed with the first (f_1) and second (f_2) higher modes computed from the CVM-H model. We have two reasons to support our model: 1) The energy of the mode on the theoretical 'phase velocity-frequency' diagram for our resulting velocity structure agrees with the observations (Fig. 6); 2) Fundamental Love and Rayleigh wave group DC are also in good agreement with the estimated velocities; however the fit to higher Rayleigh mode group DCs is not as good. This might be due to the presence of several osculation points where energy leaks between the modes [*Tokimatsu et al.*, 1992]. The phase diagram presents several measurements (blue points) between in the 0.1 and 0.2 Hz that are not fit by the Rayleigh DC in opposition to the DC associated with the CVM-H model (2). These points might be associated with surface wave reflection since there are not present in the data associated to neighbour stations.

The V_S profile is given in log-log scale in order to facilitate comparison with the original V_S profile from CVM-H model. Our V_S profile is higher by about 20% for the upper first kilometer. At greater depths both models agree well. Because of the log scale, the size of the layers in our model appear similar with depth, meaning that the solution

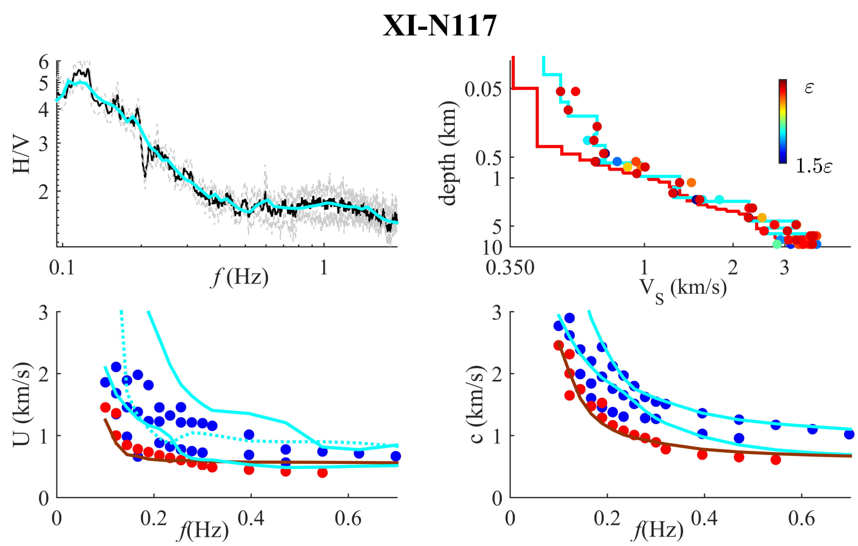

Figure 7. Top left: Experimental H/V (black line) with its lower and upper bonds (gray lines) and best H/V given by the inversion (cyan). Top right: original CVM-H (red) and optimized (cyan) models for V_S profile at station XI-N117 in function of depth. The points around the optimized profile represents alternative models with a misfit within 1 to 1.5 times best misfit. Bottom: Measured (points) and theoretical (lines) Rayleigh (blue points and cyan lines) and Love's (red points and brown lines) for group (left) and phase (right) velocities.

has thicker layers with depth. The confidence interval (obtained by the models having a misfit error 50% larger than the best solution) is also larger with increasing depth. This is due to the loss of sensitivity of our method with depth. Nonetheless, this result demonstrates the possibility to obtain a structure to 10 km, which is the deepest structure yet inferred using the H/V technique.

4.2 2D V_S model along the LASSIE array

Now that we have established that our approach retrieves reliable results where the CVM-H model is in relatively good agreement with the observed data, we carried out the inversion for all the positions to a depth of 10 km and over into a frequency band of 0.1–

2.0 Hz. Several 1D inversion results are shown in Fig. 8 and the full section of the shear velocity along the profile A–A' is presented in Fig. 9. We show the results only to 6 km depth based on the confidence intervals but the 10 km limit was necessary during the inversion to avoid compensating deeper velocity structure. Indeed, the sensitivity to velocity structure between 6 to 10 km deep is still enough to contaminates shallow results if we remove the deep structure but not sufficient to ensure reliable assessment. For all the positions, the fit of the H/V and of the phase velocities are excellent. As for station XI-N117, the fit to group velocities is not straightforward to verify due to the large quantity of data, and because of the DC crossings, but in general, the fit is good for the Rayleigh and Love fundamental modes, and somewhat diminished for higher Rayleigh modes. Nonetheless, for XI-N102 and XI-N111 stations, higher ($n_{Ray} = 3$ and $n_{Ray} = 4$) modes seem also to match the data even when not considered during the inversion.

The obtained V_S models show some continuity along the line A–A'. This result is not spatially smoothed and therefore may seem less appealing than the CVM-H model, which is smoothed both horizontally and vertically. We preferred showing it without smoothing to convey the details shown on individual V_S profiles shown in figure 7 and 8. Note that the V_S velocity in CVM-H was largely inferred from the P-wave velocity from the industry, such that much of the detail reflects V_P and is less well constrained for absolute V_S. In contrast, our model provide new direct measurements on the shear velocity. The best agreement with the CVM-H is obtained for station XI-N111. Our results validate the H/V technique with real data and with model obtained from other techniques. To our knowledge, this is the first time that a validation of the H/V technique under diffuse field assumption is reported for such deep structure. The largest discrepancy occurs for latitude higher than 34° (right part of the figure 9) and in particular for ZY-A144 station measurements. It can be seen on the group and phase velocity graphics (Fig. 8), that at this location more DC points are visible than elsewhere, and more strikingly, these points depict several Love modes. We suspect that some of these points are the consequence of surface wave scattering due to lateral heterogeneities such the Whittier hill. Since the reflections are delayed with respect to the direct arrivals, it is normal that our DCs converge toward the points with the highest apparent velocities. This suggests that the use of joint DC and H/V inversion allows identifying wave reflected on lateral heterogeneity.

5 Perspective: Assessing the Moho depth

Although we limited the depth of the inversion to 10 km, we show that the H/V technique has the power to assess deeper structure. Indeed, for certain stations (e.g., XI-N110. Fig. 10), the H/V confidence interval in the low frequency band (0.02–0.1) Hz is less than 30 % of its amplitude (except for the problematic frequency band previously mentioned (0.04–0.06 Hz), which suggests they can be used to conduct a reliable inversion; however, there are several complicating factors. Is that due to the station installation? As it was a temporary setup, maybe more care is required for recording correctly period > 10s?.

First, we do not have DC information in this frequency band, giving us an *a priori* much weaker constraints on the absolute velocities (section 3); however, the shallow part of the model (i.e. the 10 first km) is already well constrained by our previous inversion,

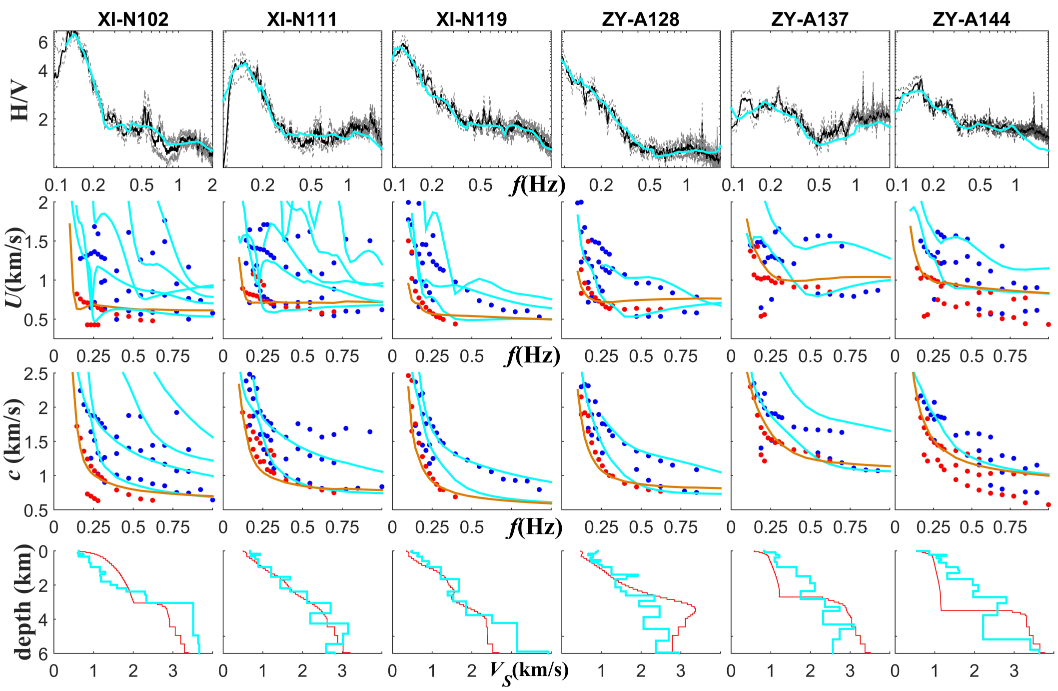

Figure 8. Examples of 1D joint inversions at different sites. The ID of the stations used is shown on top of each column. In top figure line we show the experimental H/V (black lines) with its lower and upper bounds (gray lines) and the theoretical counterpart (cyan lines). In the second and third lines, we show respectively the group and phase velocity fits with the results of FTAN average for Rayleigh velocities (blue points) and Love velocities (red points) with the theoretical DCs (cyan for Rayleigh and brown for Love). In the lower panels , we show the CVM-H model (red lines) and our estimated shear velocity model (cyan lines).

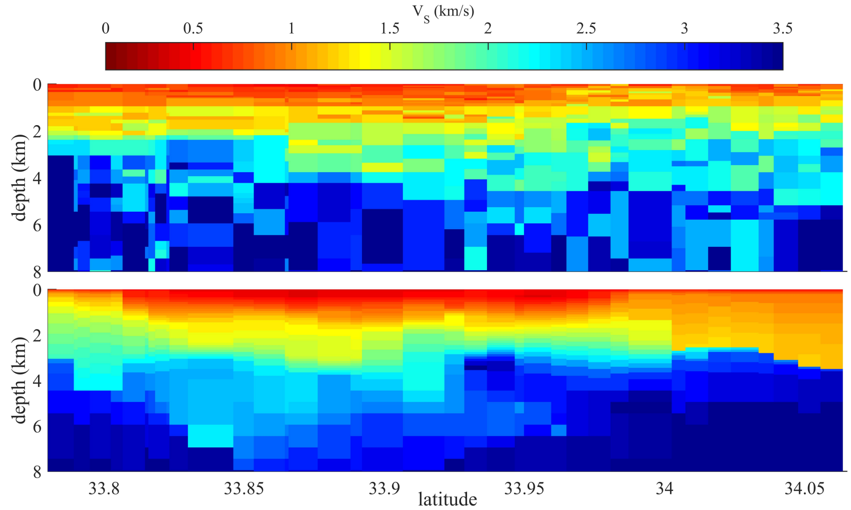

Figure 9. V_S sections along the line A–A' realized from the results of our inversion (top) and from CVM-H model bottom.

so that the results of the new inversion are expected to be only weakly biased [e.g., *Spica et al.*, 2018a].

Second, because the H/V technique is primarily more sensitive to velocity contrasts, the constant velocity indicated by the CVM-H model between 15-22 km depth is difficult to retrieve and our iterative inversion process converges to a V_S profile with several layers describing an abnormally large oscillation and large confidence interval. We modified the iterative process and further merge the layers showing large confidence intervals while only refining layers that do not.

Finally, as for station XI-N101, the two horizontal components of the energy densities have different amplitudes due to the ASF illumination being mainly unidirectional at low frequencies. As discussed in [*Perton et al.*, 2017], a solution consists in adapting the forward modelling of the H/V by considering wave propagation in a two dimensional

(2D) plane defined by the ASF illumination direction (i.e. the South-North direction noted here $\mathbf{e_{SN}}$) and the vertical direction. We projected the horizontal components of the energy densities in ($\mathbf{e_{SN}}$) direction and the results is noted H_{SN}. To allow the continuity of the H/V across the different frequency bands, we compute the H/V as $2H_{\mathrm{SN}}/V$.

The resulting observed H/V is presented in Fig. 10 along with its theoretical counterpart computed from the optimized model. To confirm that the ASF illumination is effectively 2D, we present the individual contributions $2H_{\mathrm{SN}}$ and V and compare them with the modified imaginary part of the GF (Eq. 3). Because of the presence of an unknown coefficient of proportionality in Eq. 3, these curves are all normalized by a constant and their maxima are all equal to one in the high frequency part [*Perton et al.*, 2017]. The high frequency part ($f > 0.1$ Hz) is obtained with $D = 1$ and fits well the observed data. For the low frequency part ($f \leq 0.1$ Hz), we present the results obtained with $D = 2$ (continuous line) and with $D = 1$ (dashed line). Besides the presence of the large oscillations, it is clear that only the simulation with $D = 2$, i.e. assuming 2D wave propagation, allows retrieving the trend of the data. The comparison of the individual H and V component allows us to characterize the degree of diffusivity of the ASF illumination. On the other hand, the theoretical H/V computed with $D = 2$ and with $D = 1$ in a horizontally unbounded medium are nearly identical, supporting the idea that computing H/V from ASF does not require a perfectly isotropic illumination. This is a remarkable advantage comparing to ASF cross-correlation techniques using two separated receivers, in which un-isotropic illumination might strongly be detrimental to the results [*Bensen et al.*, 2007; *Tsai*, 2009].

The resulting V_S profile is very similar to the CVM-H model between 7–30 km. Also, the Moho depth is well retrieved by our inversion (at approximately 22 km). We take care of imposing several layers around the discontinuity in order to allow the depth assessment since the thicknesses are not optimized. Although this model suffers from weak sensitivity to absolute velocity, it confirms that we can retrieve the depth of strong and deep impedance contrast across the Moho by the H/V method. This result suggests that low frequency H/V could be used as a tool to regularize the depth of deep interfaces, such as receiver functions are used in other studies. The main advantage of H/V over receiver functions is that it can be performed with temporary array (only few days of data) to obtain the necessary information, and does not rely on recording large teleseismic earthquakes for signals.

6 Conclusion

We used data from a dense, short duration broadband array that was deployed across the LAB to image the V_S structure of the basin based on a diffuse field approach. We computed multimode DCs for both Rayleigh and Love waves and also H/V spectral ratios. We extracted phase and group DCs from cross-correlation of ASF and H/Vs from its autocorrelation. These five sets of measurements were inverted jointly to assess the 1D velocity structure at each of the 40 sites of the linear array. The joint use of these measurements helps reduce the degree of nonuniqueness and gives enhanced depth sensitivity to the model. The resulting velocity model gives new and independent constraints on the V_S velocity for an area for which S-wave velocity was previously largely inferred from P-wave velocity.

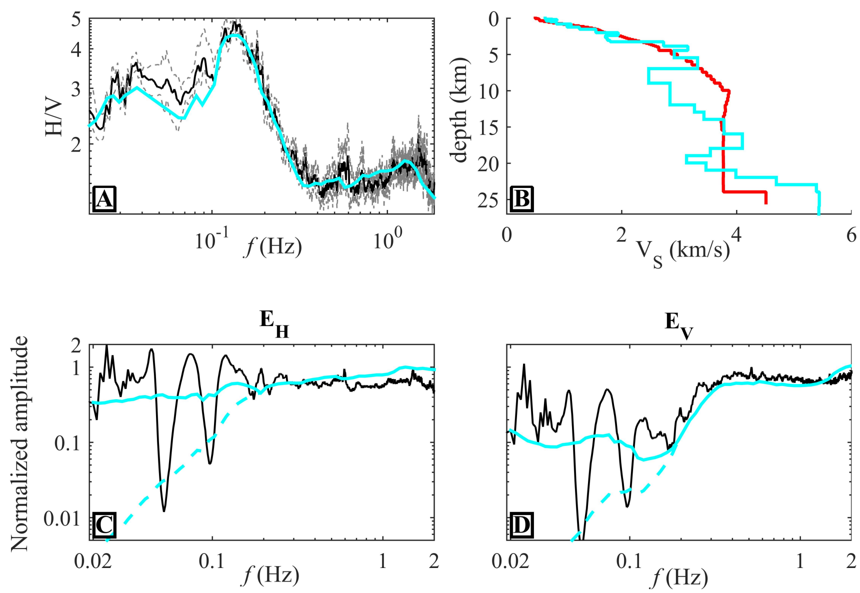

Figure 10. Example of 1D inversion at XI-N110 station that includes low frequencies. **A)** Experimental H/V (black line) with its lower and upper bonds (gray lines) and best H/V given by the inversion (cyan). **B)** original CVM-H (red) and optimized (cyan) V_S models in function of depth. Bottom: Experimental energy densities (black lines) for horizontal component **C)** and vertical component **D)** along with their respective theoretical counterpart (cyan). These latter correspond to the imaginary parts of the GF times frequency raised to a power of one above 0.2 Hz. Below that frequency, the power is equal to 1 (dashed line) or 2 (continuous line). All the energy densities are normalized to one in the frequency band 0.2–2 Hz.

At certain positions our model agrees extremely well with CVM-H model, confirming both the utility of the diffuse field H/V measurements for deep structural characterization and the predictive value of the CVM-H community velocity model in the Los Angeles region. Although our analysis yields a consistent structural picture of the subsurface in agreement with the field data, it also highlights a large degree of vertical and lateral heterogeneity in the shallow subsurface. Finally, analysis of low frequency peak in the H/V ratio showed promising results toward Moho depth characterization using such method.

7 Acknowledgments

We thank Jorge Castillo Castellanos for providing us the Green's functions computed by Yiran Ma. This research was funded by Southern California Earthquake Center (SCEC) Award #17031. We thank the partners of the LASSIE survey: Nodalseismic (Dan Hollis and Mitchell Barklage), USGS (Elizabeth Cochran), UCLA (Paul Davis) and CalPoly Pomona (J. Polet).

References

Arai, H., and K. Tokimatsu (2004), S-wave velocity profiling by inversion of microtremor H/V spectrum, *Bulletin of the Seismological Society of America*, *94*(1), 53–63, doi:10.1785/0120030028.

Bensen, G. D., M. H. Ritzwoller, M. P. Barmin, A. L. Levshin, F. Lin, M. P. Moschetti, N. M. Shapiro, and Y. Yang (2007), Processing seismic ambient noise data to obtain reliable broad-band surface wave dispersion measurements, *Geophysical Journal International*, *169*(3), 1239–1260, doi:10.1111/j.1365-246X.2007.03374.x.

Berteussen, K. A. (1977), Moho depth determinations based on spectral-ratio analysis of NORSAR long-period P waves, *Physics of the Earth and Planetary Interiors*, *15*(1), 13–27, doi:10.1016/0031-9201(77)90006-1.

Bouchon, M. (2003), A review of the discrete wavenumber method, *Pure and applied Geophysics*, *160*(3-4), 445–465.

Bowden, D., V. Tsai, and F. Lin (2015), Site amplification, attenuation, and scattering from noise correlation amplitudes across a dense array in long beach, ca, *Geophysical Research Letters*, *42*(5), 1360–1367.

Brocher, T. M. (2005), Empirical relations between elastic wavespeeds and density in the Earth's crust, *Bulletin of the Seismological Society of America*, *95*(6), 2081–2092.

Byrd, R. H., M. E. Hribar, and J. Nocedal (1999), An interior point algorithm for large-scale non-linear programming, *SIAM Journal on Optimization*, *9*(4), 877–900.

Cruz-Atienza, V., J. Tago, J. Sanabria-Gómez, E. Chaljub, V. Etienne, J. Virieux, and L. Quintanar (2016), Long duration of ground motion in the paradigmatic valley of mexico, *Scientific reports*, *6*, 38,807.

Dal Moro, G. (2011), Some aspects about surface wave and HVSR analyses: a short overview and a case study., *Bollettino di Geofisica Teorica ed Applicata*, *52*(2).

Denolle, M., E. Dunham, G. Prieto, and G. Beroza (2014), Strong ground motion prediction using virtual earthquakes, *Science*, *343*(6169), 399–403.

Denolle, M. A., E. M. Dunham, and G. C. Beroza (2012), Solving the surface-wave eigenproblem with Chebyshev spectral collocation, *Bulletin of the Seismological Society of America*, *102*(3), 1214–1223.

Dziewonski, A. M., and D. L. Anderson (1981), Preliminary reference earth model, *Physics of the Earth and Planetary Interiors*, *25*(4), 297–356, doi:10.1016/0031-9201(81)90046-7.

García-Jerez, A., J. Piña-Flores, F. J. Sánchez-Sesma, F. Luzón, and M. Perton (2016), A computer code for forward calculation and inversion of the H/V spectral ratio under the diffuse field assumption, *Computers & Geosciences*, *97*, 67 – 78, doi:http://dx.doi.org/10.1016/j.cageo.2016.06.016.

Graves, R., T. H. Jordan, S. Callaghan, E. Deelman, E. Field, G. Juve, C. Kesselman, P. Maechling, G. Mehta, K. Milner, et al. (2011), Cybershake: A physics-based seismic hazard model for southern california, *Pure and Applied Geophysics*, *168*(3-4), 367–381.

Hauksson, E. (2000), Crustal structure and seismicity distribution adjacent to the pacific and north america plate boundary in southern california, *Journal of Geophysical Research: Solid Earth*, *105*(B6), 13,875–13,903.

Jennings, C., and W. Bryant (2010), Fault activity map of california: California geological survey geologic data map no. 6.

Komatitsch, D., Q. Liu, J. Tromp, P. Suss, C. Stidham, and J. H. Shaw (2004), Simulations of ground motion in the los angeles basin based upon the spectral-element method, *Bulletin of the Seismological Society of America*, *94*(1), 187–206.

LASSIE (2014), Los angeles seismic syncline interferometry experiment, caltech, dataset, doi:doi:10.7909/C3FX77K9.

Lee, E.-J., P. Chen, T. H. Jordan, P. B. Maechling, M. A. Denolle, and G. C. Beroza (2014), Full-3-d tomography for crustal structure in southern california based on the scattering-integral and the adjoint-wavefield methods, *Journal of Geophysical Research: Solid Earth*, *119*(8), 6421–6451.

Lin, F.-C., D. Li, R. W. Clayton, and D. Hollis (2013), High-resolution 3D shallow crustal structure in Long Beach, California: Application of ambient noise tomography on a dense seismic array, *Geophysics*, *78*(4), Q45–Q56.

Liu, X., and Y. Ben-Zion (2017), Analysis of non-diffuse characteristics of the seismic noise field in southern california based on correlations of neighbouring frequencies, *Geophysical Journal International*, *212*(2), 798–806.

Lontsi, A. M., F. J. Sánchez-Sesma, J. C. Molina-Villegas, M. Ohrnberger, and F. Krüger (2015), Full microtremor H/V (z, f) inversion for shallow subsurface characterization, *Geophysical Journal International*, *202*(1), 298–312.

Lontsi, A. M., M. Ohrnberger, F. Krüger, and F. J. Sánchez-Sesma (2016), Combining surface-wave phase-velocity dispersion curves and full microtremor horizontal-to-vertical spectral ratio for subsurface sedimentary site characterization, *Interpretation*, *4*(4), SQ41–SQ49.

Ma, Y., and R. W. Clayton (2016), Structure of the los angeles basin from ambient noise and receiver functions, *Geophysical Journal International*, *206*(3), 1645–1651.

Ma, Y., R. W. Clayton, and D. Li (2016), Higher-mode ambient-noise rayleigh waves in sedimentary basins, *Geophysical Journal International*, *206*(3), 1634–1644.

Magistrale, H., K. McLaughlin, and S. Day (1996), A geology-based 3d velocity model of the los angeles basin sediments, *Bulletin of the Seismological Society of America*, *86*(4), 1161–1166.

Magistrale, H., S. Day, R. W. Clayton, and R. Graves (2000), The scec southern california reference three-dimensional seismic velocity model version 2, *Bulletin of the Seismological Society of America*, *90*(6B), S65–S76.

Maufroy, E., P. Lacroix, E. CHALJUB, C. SIRA, G. GRELLE, L. BONITO, M. CAUSSE, V. M. CRUZ-ATIENZA, F. HOLLENDER, F. COTTON, and P.-Y. BARD (2018), Towards rapid prediction of topographic amplification at small scales: contribution of the 'fsc' proxy and pléiades terrain models for the 2016 amatrice earthquake (italy, mw 6.0), in *16th european conferance on Eartquake Engineering*.

Molina-Villegas, J. C., J. D. Jaramillo Fernández, J. Piña-Flores, and F. J. Sánchez-Sesma (2018), Local generation of love surface waves at the edge of a 2d alluvial valleylocal generation of love surface waves at the edge of a 2d alluvial valley, *Bulletin of the Seismological Society of America*, *108*(4), 2090, doi:10.1785/0120170360.

Nakamura, Y. (1989), A method for dynamic characteristics estimation of subsurface using microtremor on the ground surface, *Railway Technical Research Institute, Quarterly Reports*, *30*(1).

Nakata, N., J. P. Chang, J. F. Lawrence, and P. Boué (2015), Body wave extraction and tomography at Long Beach, California, with ambient-noise interferometry, *Journal of Geophysical Research: Solid Earth*, *120*(2), 1159–1173, doi:10.1002/2015JB011870.

Olsen, K. (2000), Site amplification in the los angeles basin from three-dimensional modeling of ground motion, *Bulletin of the Seismological Society of America*, *90*(6B), S77–S94.

Olsen, K., S. Day, J. Minster, Y. Cui, A. Chourasia, M. Faerman, R. Moore, P. Maechling, and T. Jordan (2006), Strong shaking in los angeles expected from southern san andreas earthquake, *Geophysical Research Letters*, *33*(7).

Olsen, K., S. Day, L. Dalguer, J. Mayhew, Y. Cui, J. Zhu, V. Cruz-Atienza, D. Roten, P. Maechling, T. Jordan, et al. (2009), Shakeout-d: Ground motion estimates using an ensemble of large earthquakes on the southern san andreas fault with spontaneous rupture propagation, *Geophysical Research Letters*, *36*(4).

Parolai, S., M. Picozzi, S. Richwalski, and C. Milkereit (2005), Joint inversion of phase velocity dispersion and H/V ratio curves from seismic noise recordings using a genetic algorithm, considering higher modes, *Geophysical research letters*, *32*(1).

Perton, M., and F. J. Sánchez-Sesma (2016), Green's function calculation from equipartition theorem, *The Journal of the Acoustical Society of America*, *140*(2), 1309–1318.

Perton, M., F. J. Sánchez-Sesma, A. Rodríguez-Castellanos, M. Campillo, and R. L. Weaver (2009), Two perspectives on equipartition in diffuse elastic fields in three dimensions, *The Journal of the Acoustical Society of America*, *126*(3), 1125–1130, doi: 10.1121/1.3177262.

Perton, M., Z. Spica, and C. Caudron (2017), Inversion of the horizontal to vertical spectral ratio in presence of strong lateral heterogeneity, *Geophysical Journal International*.

Piña-Flores, J., M. Perton, A. García-Jerez, E. Carmona, F. Luzón, J. C. Molina-Villegas, and F. J. Sánchez-Sesma (2016), The inversion of spectral ratio H/V in a layered system using the Diffuse Field Assumption (DFA), *Geophysical Journal International*, doi:10.1093/gji/ggw416.

Rivet, D., M. Campillo, F. Sanchez-Sesma, N. M. Shapiro, and S. K. Singh (2015), Identification of surface wave higher modes using a methodology based on seismic noise and coda waves, *Geophysical Journal International*, *203*(2), 856–868.

Roux, P., and Y. Ben-Zion (2017), Rayleigh phase velocities in southern california from beamforming short-duration ambient noise, *Geophysical Journal International*, *211*(1), 450–454, doi:10.1093/gji/ggx316.

Sánchez-Sesma, F. J., M. Rodríguez, U. Iturrarán-Viveros, F. Luzón, M. Campillo, L. Margerin, A. García-Jerez, M. Suarez, M. A. Santoyo, and A. Rodríguez-Castellanos (2011), A theory for microtremor H/V spectral ratio: application for a layered medium, *Geophysical Journal International*, *186*(1), 221–225, doi:10.1111/j.1365-246X.2011.05064.x.

Savage, M. K., F.-C. Lin, and J. Townend (2013), Ambient noise cross-correlation observations of fundamental and higher-mode rayleigh wave propagation governed by basement resonance, *Geophysical Research Letters*, *40*(14), 3556–3561.

Scherbaum, F., K.-G. Hinzen, and M. Ohrnberger (2003), Determination of shallow shear wave velocity profiles in the Cologne, Germany area using ambient vibrations, *Geophysical Journal International*, *152*(3), 597–612.

Shapiro, N., and M. Ritzwoller (2002), Monte-Carlo inversion for a global shear-velocity model of the crust and upper mantle, *Geophysical Journal International*, *151*(1), 88–105, doi:10.1046/j.1365-246X.2002.01742.x.

Shapiro, N. M., M. Campillo, L. Stehly, and M. H. Ritzwoller (2005), High-resolution surface-wave tomography from ambient seismic noise, *Science*, *307*(5715), 1615–1618, doi:10.1126/science.1108339.

Shaw, J. H., A. Plesch, C. Tape, M. P. Suess, T. H. Jordan, G. Ely, E. Hauksson, J. Tromp, T. Tanimoto, R. Graves, et al. (2015), Unified structural representation of the southern california crust and upper mantle, *Earth and Planetary Science Letters*, *415*, 1–15.

Spica, Z., C. Caudron, M. Perton, T. Lecocq, T. Camelbeeck, D. Legrand, J. Piña-Flores, A. Iglesias, and D. K. Syahbana (2015), Velocity models and site effects at Kawah Ijen volcano and Ijen caldera (Indonesia) determined from ambient noise cross-correlations and directional energy density spectral ratios, *Journal of Volcanology and Geothermal Research*, *302*, 173–189, doi:10.1016/j.jvolgeores.2015.06.016.

Spica, Z., M. Perton, M. Calò, D. Legrand, F. Córdoba-Montiel, and A. Iglesias (2016), 3-D shear wave velocity model of Mexico and south US: bridging seismic networks with ambient noise cross-correlations (C^1) and correlation of coda of correlations (C^3), *Geophysical Journal International*, *206*(3), 1795–1813, doi:10.1093/gji/ggw240.

Spica, Z., M. Perton, and D. Legrand (2017a), Anatomy of the Colima volcano magmatic system, Mexico, *Earth and Planetary Science Letters*, *459*, 1–13, doi:10.1016/j.epsl.2016.11.010.

Spica, Z., M. Perton, N. Nakata, X. Liu, and G. C. Beroza (2018a), Shallow vs imaging of the groningen area from joint inversion of multimode surface waves and h/v spectral ratios, *Seismological Research Letters*.

Spica, Z. J., M. Perton, N. Nakata, X. Liu, and G. C. Beroza (2017b), Site characterization at Groningen gas field area through joint surface-borehole H/V analysis, *Geophysical Journal International*, *212*(1), 412–421, doi:10.1093/gji/ggx426.

Spica, Z. J., N. Nakata, X. Liu, T. Zijian, X. Campman, and G. C. Beroza (2018b), The ambient seismic field at Groningen gas field: An overview from the surface to reservoir depth, *Seismological Research Letters*.

Süss, M. P., and J. H. Shaw (2003), P wave seismic velocity structure derived from sonic logs and industry reflection data in the los angeles basin, california, *Journal of Geophysical Research: Solid Earth*, *108*(B3).

Tanimoto, T., and L. Rivera (2005), Prograde rayleigh wave particle motion, *Geophysical Journal International*, *162*(2), 399–405, doi:10.1111/j.1365-246X.2005.02481.x.

Tape, C., Q. Liu, A. Maggi, and J. Tromp (2009), Adjoint tomography of the southern california crust, *Science*, *325*(5943), 988–992.

Tokimatsu, K., S. Tamura, and H. Kojima (1992), Effects of multiple modes on rayleigh wave dispersion characteristics, *Journal of Geotechnical Engineering*, *118*(10), 1529–1543, doi:10.1061/(ASCE)0733-9410(1992)118:10(1529).

Tomar, G., E. Stutzmann, A. Mordret, J.-P. Montagner, S. C. Singh, and N. M. Shapiro (2018), Joint inversion of first overtone and fundamental mode for deep imaging at the valhall oil field using ambient noise, *Geophysical Journal International*.

Tsai, V. C. (2009), On establishing the accuracy of noise tomography travel-time measurements in a realistic medium, *Geophysical Journal International*, *178*(3), 1555–1564, doi:10.1111/j.1365-246X.2009.04239.x.

Wald, D. J., and R. W. Graves (1998), The seismic response of the los angeles basin, california, *Bulletin of the Seismological Society of America*, *88*(2), 337–356.

Wright, T. L. (1991), Structural geology and tectonic evolution of the los angeles basin, california, *Act. Margin Basins*, *52*, 35–134.

Xie, J., M. H. Ritzwoller, W. Shen, Y. Yang, Y. Zheng, and L. Zhou (2013), Crustal radial anisotropy across eastern Tibet and the western Yangtze craton, *Journal of Geophysical Research: Solid Earth*, *118*(8), 4226–4252, doi:10.1002/jgrb.50296.

Zhu, L., and H. Kanamori (2000), Moho depth variation in southern california from teleseismic receiver functions, *Journal of Geophysical Research: Solid Earth*, *105*(B2), 2969–2980.

Zor, E., S. Özalaybey, A. Karaaslan, M. C. Tapırdamaz, S. Ç. Özalaybey, A. Tarancıoğlu, and B. Erkan (2010), Shear wave velocity structure of the Izmit Bay area (Turkey) estimated from active–passive array surface wave and single-station microtremor methods, *Geophysical Journal International*, *182*(3), 1603–1618.